SARAF Luminal Domain Structure Reveals a Novel Domain-Swapped β-Sandwich Fold Important for SOCE Modulation

Christopher R. Kimberlin[1,†], **Anna Meshcheriakova**[2,†], **Raz Palty**[3], **Adi Raveh**[2], **Izhar Karbat**[2], **Eitan Reuveny**[2] and **Daniel L. Minor Jr.**[1,4,5,6,7,8,]

1 - *Cardiovascular Research Institute,* University of California, San Francisco, CA 94148, USA
2 - *Department of Biomolecular Sciences,* Weizmann Institute of Science, Rehovot 7610001, Israel
3 - *Rappaport Family School of Medicine,* Technion-Israel Institute of Technology, Haifa 31096, Israel
4 - *Department of Biochemistry and Biophysics,* University of California, San Francisco, CA 94158, USA
5 - *Department of Cellular and Molecular Pharmacology,* University of California, San Francisco, CA 94158, USA
6 - *California Institute for Quantitative Biomedical Research,* University of California, San Francisco, CA 94158, USA
7 - *Kavli Institute for Fundamental Neuroscience,* University of California, San Francisco, San Fancisco, CA 94158, USA
8 - *Molecular Biophysics and Integrated Bioimaging Division,* Lawrence Berkeley National Laboratory, Berkeley, CA 94720, USA

Correspondence to Eitan Reuveny and Daniel L. Minor: Cardiovascular Research Institute, University of California, San Francisco, CA 94158, USA. e.reuveny@weizmann.ac.il, daniel.minor@ucsf.edu
https://doi.org/10.1016/j.jmb.2019.05.008
Edited by James Bowie

Abstract

Store-Operated Calcium Entry (SOCE) plays key roles in cell proliferation, muscle contraction, immune responses, and memory formation. The coordinated interactions of a number of proteins from the plasma and endoplasmic reticulum membranes control SOCE to replenish internal Ca^{2+} stores and generate intracellular Ca^{2+} signals. SARAF, an endoplasmic reticulum resident component of the SOCE pathway having no homology to any characterized protein, serves as an important brake on SOCE. Here, we describe the X-ray crystal structure of the SARAF luminal domain, $SARAF_L$. This domain forms a novel 10-stranded β-sandwich fold that includes a set of three conserved disulfide bonds, denoted the "SARAF-fold." The structure reveals a domain-swapped dimer in which the last two β-strands (β9 and β10) are exchanged forming a region denoted the "SARAF luminal switch" that is essential for dimerization. Sequence comparisons reveal that the SARAF-fold is highly conserved in vertebrates and in a variety of pathologic fungi. Förster resonance energy transfer experiments using full-length SARAF validate the formation of the domain-swapped dimer in cells and demonstrate that dimerization is reversible. A designed variant lacking the SARAF luminal switch shows that the domain swapping is essential to function and indicates that the SARAF dimer accelerates SOCE inactivation.

© 2019 Elsevier Ltd. All rights reserved.

Calcium is a potent second messenger required for diverse cellular signaling processes that occur over a wide range of timescales such as vesicle release (μs), fertilization (minutes), and proliferation and apoptosis (hours) [1,2]. Consequently, cells use a multitude of systems to control cytoplasmic Ca^{2+} level changes. Signaling in both non-excitable and excitable cells is frequently initiated by stimulation of a G-protein coupled receptors and receptor tyrosine kinases [3,4] that trigger inositol triphosphate (IP_3)-mediated release of Ca^{2+} from intracellular stores. The resulting intracellular Ca^{2+} store depletion activates a process called Store-Operated Calcium Entry (SOCE) that works to replenish the internal Ca^{2+} stores and that affects a range of responses, such as proliferation, transcription, and cell motility [5–9].

The prototypical mediator of SOCE is the calcium release-activated calcium (CRAC) channel formed by the plasma membrane (PM) pore-forming subunit, Orai, and an endoplasmic reticulum (ER) Ca^{2+} sensor and channel activator, STIM [10–13]. Both SOCE components have multiple isoforms of which the best studied are STIM1 and Orai1. SOCE activation involves an elegant mechanism that results in the clustering of both STIM and Orai at

the ER–PM junctions [14–16]. Depletion of ER Ca^{2+} induces STIM1 oligomerization and translocation to the ER–PM junctions, where it binds to Orai1 and initiates Ca^{2+} influx [17–22]. Once SOCE is initiated, Ca^{2+} from CRAC channels initiates autoregulatory deactivation and inactivation processes that shape the duration and magnitude of the Ca^{2+} signal. Two types of Ca^{2+} dependent inactivation have been described: a fast process that occurs on the millisecond time scale, and a slow process that develops over multiple minutes [23]. The ER resident, single-pass transmembrane SARAF [24] (for *S*OCE-*A*ssociated *R*egul*A*tory *F*actor) is a central facilitator of the slow Ca^{2+} dependent inactivation of CRAC channels.

SARAF lacks homology to any known protein. Previous studies established that the SARAF elements on either side of the membrane encode two distinct functions. The SARAF cytosolic domain is required for driving SOCE inactivation through inter-action with STIM [24–26], whereas the luminal domain regulates SOCE inactivation by responding to changes in ER Ca^{2+} levels [24]. Here, we present the X-ray crystal structure of the SARAF ER luminal domain, $SARAF_L$. This domain forms a domain-swapped dimer arrangement built from a novel β-sandwich fold that we term the "SARAF fold." Cross-linking, analytical ultracentrifugation, and Förster resonance energy transfer (FRET) experiments demonstrate that self-association of $SARAF_L$ and full-length SARAF in cells depends on the domain-swapped element denoted as the "SARAF luminal switch." Finally, CRAC current recording in cells that express wild-type SARAF or dimerization-incompetent SARAF shows that self-association via the SARAF luminal switch is critical for control of CRAC currents.

Results

SARAF luminal domain dimerizes using a novel, conserved domain-swapped β-sandwich fold

The SARAF ER luminal domain contains six cysteines and bears no sequence homology to any protein of known structure (Fig. 1a and b). Therefore, we set out to define its structure to gain insight into how it might affect SOCE. Extensive screening identified a human SARAF luminal domain construct that could be expressed in *Escherichia coli* Shuffle Express cells, purified to homogeneity, and crystallized. This construct, denoted $SARAF_L$, excludes the N-terminal signal peptide, encompasses luminal domain residues 30–164, and ends eight residues before the putative transmembrane helix [24,27] (Fig. 1a). $SARAF_L$ crystals diffracted X-rays to a resolution of 1.9 Å, and the structure was determined by single isomorphous replacement with anomalous

scattering (SIRAS) using a single platinum derivative ($K_2Pt(NO)_4$) that diffracted X-rays to 2.15 Å (Fig. S1a, Table S1). $SARAF_L$ crystallized with two molecules in the asymmetric unit. One copy had continuous electron density from N- to C-terminus, while the other showed short regions of disorder between residues 88–93 and 149–156 (Fig. S1b). Hence, the structural description focuses on the complete copy.

$SARAF_L$ forms a domain-swapped dimer comprising a 10 β-strand barrel having three conserved disulfides (Fig. 1b–d). There are two well-ordered extended loops that connect β2–β4 and β6–β8. Both are stabilized by the presence of a short intervening β-strand midway through the loop that forms β-sheet interactions with other β-strands (Fig. 1c and d). The β3 strand in the middle of the β2–β4 loop makes a parallel β-sheet with β8, whereas the β7 strand in the β6–β8 loop forms an anti-parallel interaction with β1. The β2–β4 and β6–β8 loops are further constrained by the Cys66–Cys73 and Cys114–Cys130 disulfides, respectively. The remaining disulfide, Cys83–Cys97, is buried in the core of the protein and links β4 and β5. There is a single α-helix, α1, that follows β8. This helix extends from the body of the structure and mediates a domain swap through which β-strands β9 and β10 complete the β-sheet fold of the other member of the dimer (Fig. 1e).

The domain-swapped β9–β10 element comprising Gln152–Lys164 makes extensive interactions with the $SARAF_L$ core that are mediated by the formation of anti-parallel β-sheet main chain hydrogen bonds between β9–β5 and a short parallel β-sheet made between β10 and β6 and that bury 2232 $Å^2$ per tail-body interface. (Fig. 1c–e). The backbone β-sheet interactions are accompanied by a number of side-chain-mediated interactions. Cross-strand hydrogen bonds are formed by His153–Tyr105 (Fig. S1c), a network comprising Ser157, Ser159, and Thr110 (Fig. S1d), and a Try163 hydroxyl and Tyr91 carbonyl interaction (Fig. 1e). Phe155 and Phe158 sidechains rest in shallow grooves on the surface the $SARAF_L$ core, while the Tyr161 sidechain is buried in a largely hydrophobic pocket (Fig. 1e). Finally, the Lys164 C-terminal carboxylate forms a hydrogen bond to the amide of Gly116 and salt-bridge with the Arg57 sidechain (Fig. 1e). Despite being involved in a Ca^{2+}-dependent process, SARAF lacks any obvious Ca^{2+}-binding motifs [24]. Examination of the surface electrostatic potential (Fig. 2) revealed a few disperse regions of negative potential, but none that would indicate a site for Ca^{2+}-binding, as well as a large positive patch in a pocket near SS3. In accordance with this lack of clear Ca^{2+}-binding motifs, even though the structure was determined in the presence of 1 mM $CaCl_2$, we found no crystallographic evidence for Ca^{2+} binding to $SARAF_L$.

Searches for structural homology between $SARAF_L$ and proteins of known structure using the DALI database [28] revealed no strong matches,
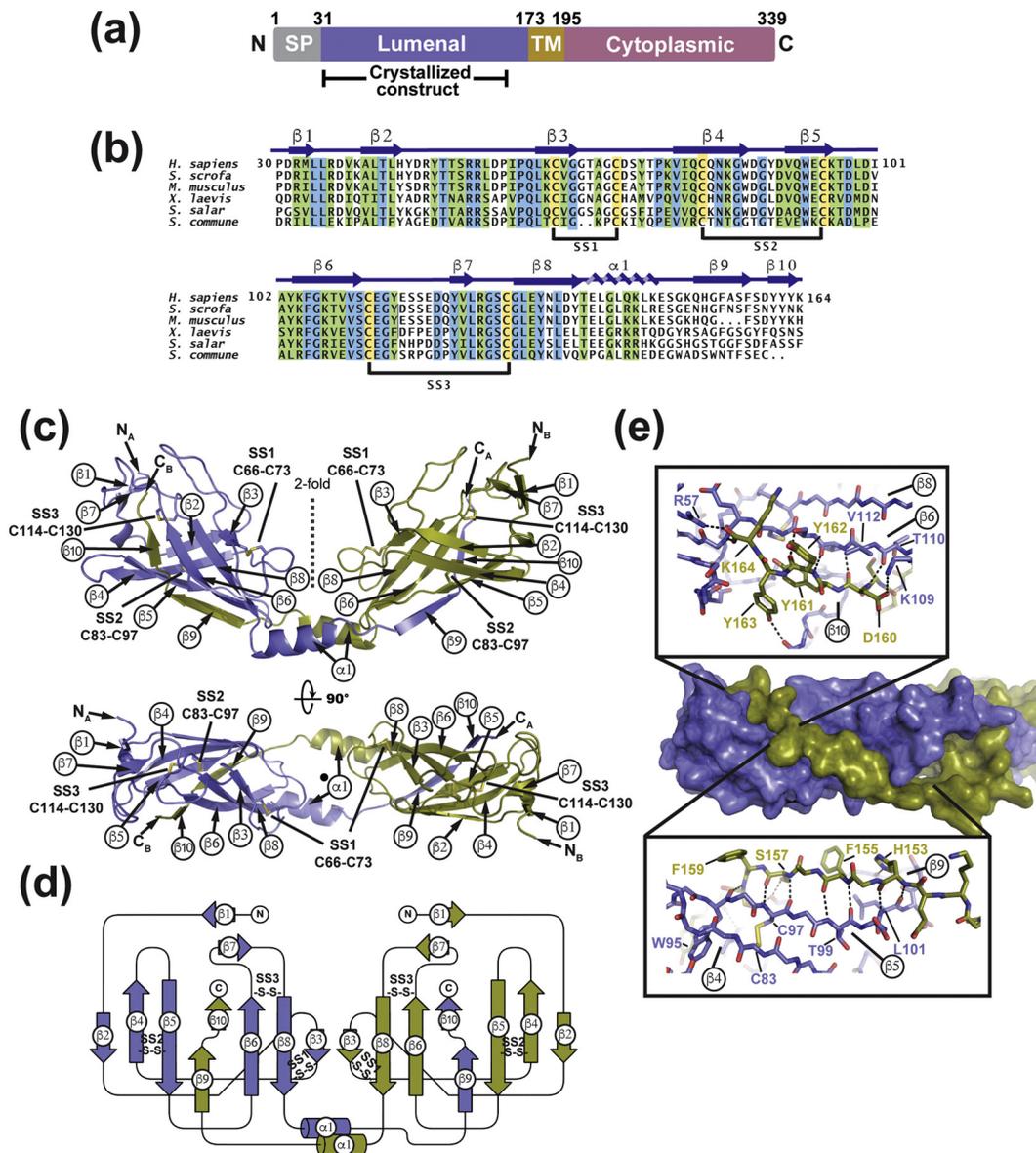
Fig. 1. Structure of SARAF_L. (a) SARAF schematic. Signal peptide (SP, gray), luminal (purple), transmembrane (TM, brown), and cytoplasmic (magenta) domains and amino acid boundaries of each are indicated. Extent of crystallized SARAF_L construct is shown. (b) SARAF_L sequence comparison from human (*H. sapiens*), pig (*S. scrofa*), mouse (*M. musculus*), frog (*X. laevis*), salmon (*S. salar*), and mushroom (*S. commune*). Invariant (blue), conserved (green) and cysteines (yellow) are highlighted. Secondary structure elements and disulfide bonds (SS1, SS2, and SS3) are shown. (c) Structure of the SARAF_L domain-swapped dimer. N and C termini (N_A, N_B, C_A, and C_B) and secondary structure elements of each chain are labeled. Disulfide bonds are shown as sticks and are labeled. Chains A and B are slate and deep olive, respectively. (d) SARAF_L domain-swapped dimer topology diagram. "S–S" denotes disulfide bonds. (e) Detailed view of interactions of domain-swapped β9 and β10 with the SARAF_L core. Dashed lines indicate hydrogen bonds.

indicating that SARAF_L has a unique fold. Relaxation of the similarity criteria to allow for a generous Z-score cutoff (>2) identified a set of β-sheet structures that include the γ-COPI appendage domain (1R4X), Xenavidin (2UYW), Avidin-related protein 2 (1WBI), and a conserved domain from *Bacillus anthracis* (3FBQ) (Z-scores of 2.3, 2.2, 2.1, and 2.0, respectively)(Fig. 3). However, strand connectivity analysis reveals that SARAF_L is substantially different from each of these folds. Namely, SARAF_L lacks the Greek-key motif of Xenavidin and Avidin-related protein 2, and is not composed of strictly anti-parallel β-sheets as are the γ-COPI appendage domain and the *B. anthracis* conserved domain. Hence, SARAF_L has a novel β-sandwich architecture that we now call the SARAF-fold.
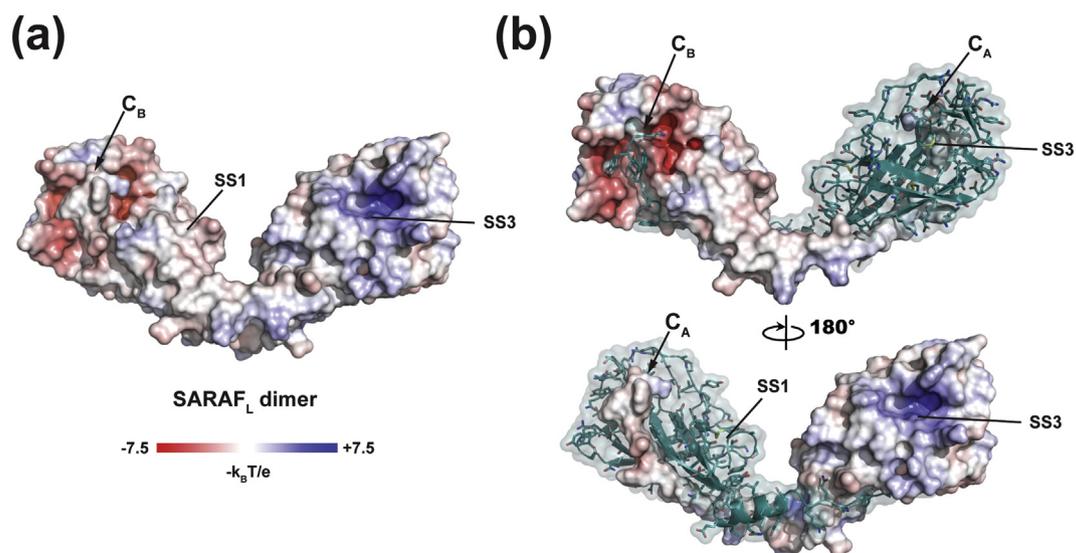
Fig. 2. SARAF$_L$ electrostatic surface potential. (a) Electrostatic surface potential for the SARAF$_L$ dimer calculated in 150-mM ionic strength. (a) Electrostatic surface potential for one monomer of the SARAF$_L$ dimer. In both panels, select elements are labeled.

Analysis of >90 SARAF$_L$-related sequences uncovers a set of related proteins spanning all five vertebrate classes (mammals, birds, amphibians, fish, and reptiles), including some very ancient animals such as the sea lamprey (*Petromyzon marinus*) and coelacanth (*Latimeria chalumnae*). This family of SARAF$_L$ homologs has strong conservation of the six cysteines that form the three SARAF$_L$ disulfides as well as high conservation of many residues that form the core of the SARAF$_L$ fold (Figs. 1b, 4a, and S2). We did not find SARAF-like sequences among other metazoans, but, surprisingly, identified a group of transmembrane proteins similar to SARAF$_L$ in fungi, including organisms that are pathogens of mammals, insects, or plants (Fig. S3). This group of SARAF$_L$ homologs diverges more from human SARAF$_L$ than

Protein (PDB)	Z-score	RMSD (Å)	Strand order	Structure
SARAF$_L$	—	—		
γ-COPI (1R4X)	2.3	2.9		
Xenavidin (2UYW)	2.2	4.1		
Avidin related protein 2 (1WBI)	2.1	4.1		
Bacillus anthracis conserved domain (3FBQ)	2.0	3.6		

Fig. 3. Analysis of the SARAF$_L$ fold. SARAF$_L$ structural homologs identified using DALI [28]. DALI search Z-score, RMSD$_{Cα}$, diagram of strand topology, and structure are shown. Cartoon representations highlighting secondary structure elements are colored by rainbow from N-terminus (blue) to C-terminus (red).
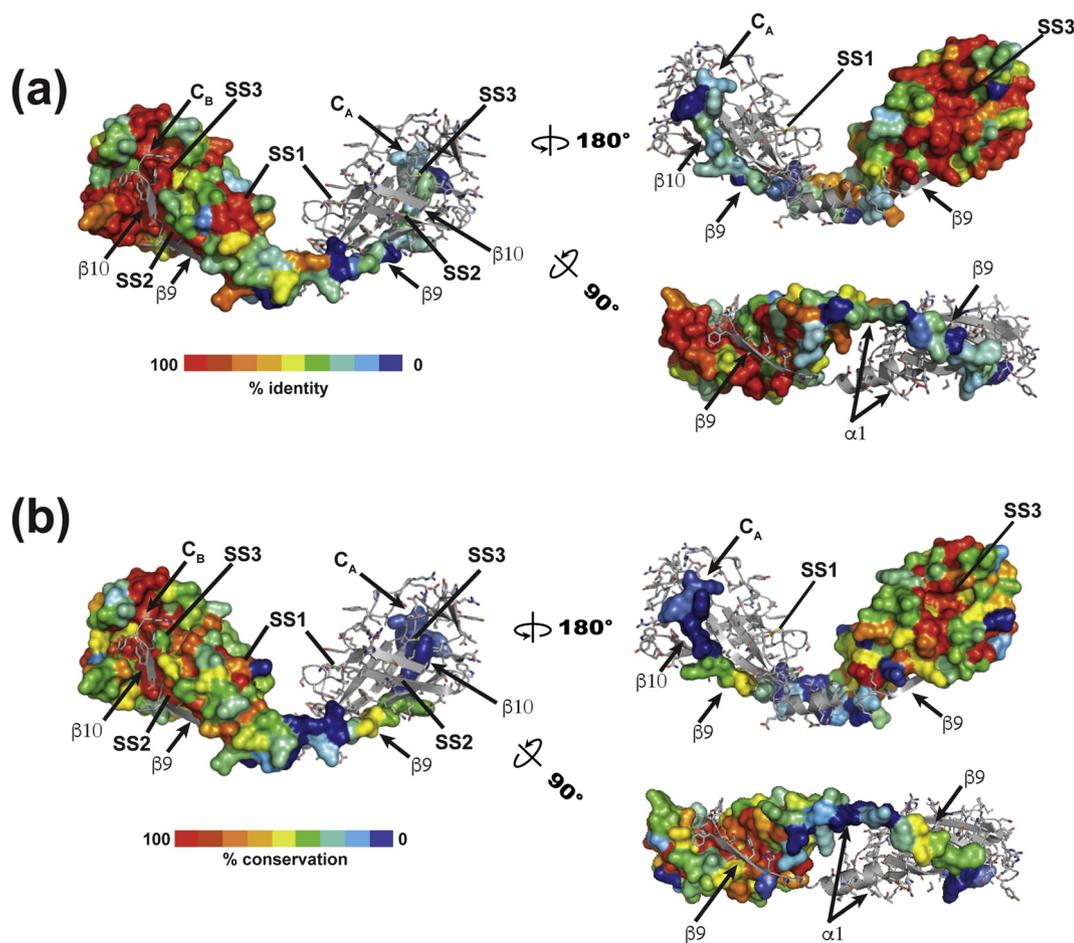
Fig. 4. Conservation mapping of vertebrate sequences on the SARAF$_L$ structure for (a) vertebrate and (b) fungal sequences. One member of the dimer is shown in surface rendering. Select structural elements are labeled.

the vertebrate sequences. For example, the exposed disulfide, SS1, lacks one of the cysteines in a small subset of the fungal sequences, and the swapped β9/β10 strand is not well conserved. Nevertheless, the data clearly identify the presence of key elements of the core SARAF$_L$ structure (Fig. 4b). The unique nature of the SARAF$_L$ structure, together with the presence of clear homologs in vertebrates and fungi, indicates that SARAF$_L$ structure represents a previously unknown, widely-occurring protein fold.

SARAF$_L$ dimerization depends on the swapped domain

The presence of the domain-swapped dimer in the crystals prompted us to investigate the nature of this interaction further. Characterization by size exclusion chromatography and multi-angle light scattering (SEC-MALS) [29] indicated the dominant presence of SARAF$_L$ monomers in solution at 64 µM (observed 15.84 ± 0.08 kDa, calculated 15.49 kDa) (Fig. 5a). Further probing with glutaraldehyde cross-linking revealed a dimeric species that appeared

with increasing protein concentrations into the 100-µM range (Fig. 5b), suggesting that the propensity to dimerize is weak. As the domain-swapped dimer observed requires an exchange of β9 and β10 (Fig. 1c and d), we created a SARAF$_L$ deletion construct truncated at residue 150 to remove the domain-swapped β-strands β9 and β10 (Δβ9/Δβ10). Expression and purification of SARAF$_L$(Δβ9/Δβ10) yielded a protein having similar properties to SARAF$_L$ running as a monomer on gel filtration (Fig. S4a and b) and having a similar circular dichroism spectrum to SARAF$_L$, indicative of a folded protein (Fig. S4c). Notably, the deletion of the domain-swapped strands, β9 and β10, dramatically diminished the ability of the protein to be crosslinked by glutaraldehyde (Fig. 5b), supporting the idea that the dimer seen in SARAF$_L$ relies on the domain swap interaction of β9 and β10.

To probe the strength of SARAF$_L$ dimer formation, we used equilibrium analytical ultracentrifugation. Fits of the SARAF$_L$ data using a single-species monomer model yielded upwardly curving residuals, particularly at the highest concentration (200 µM),
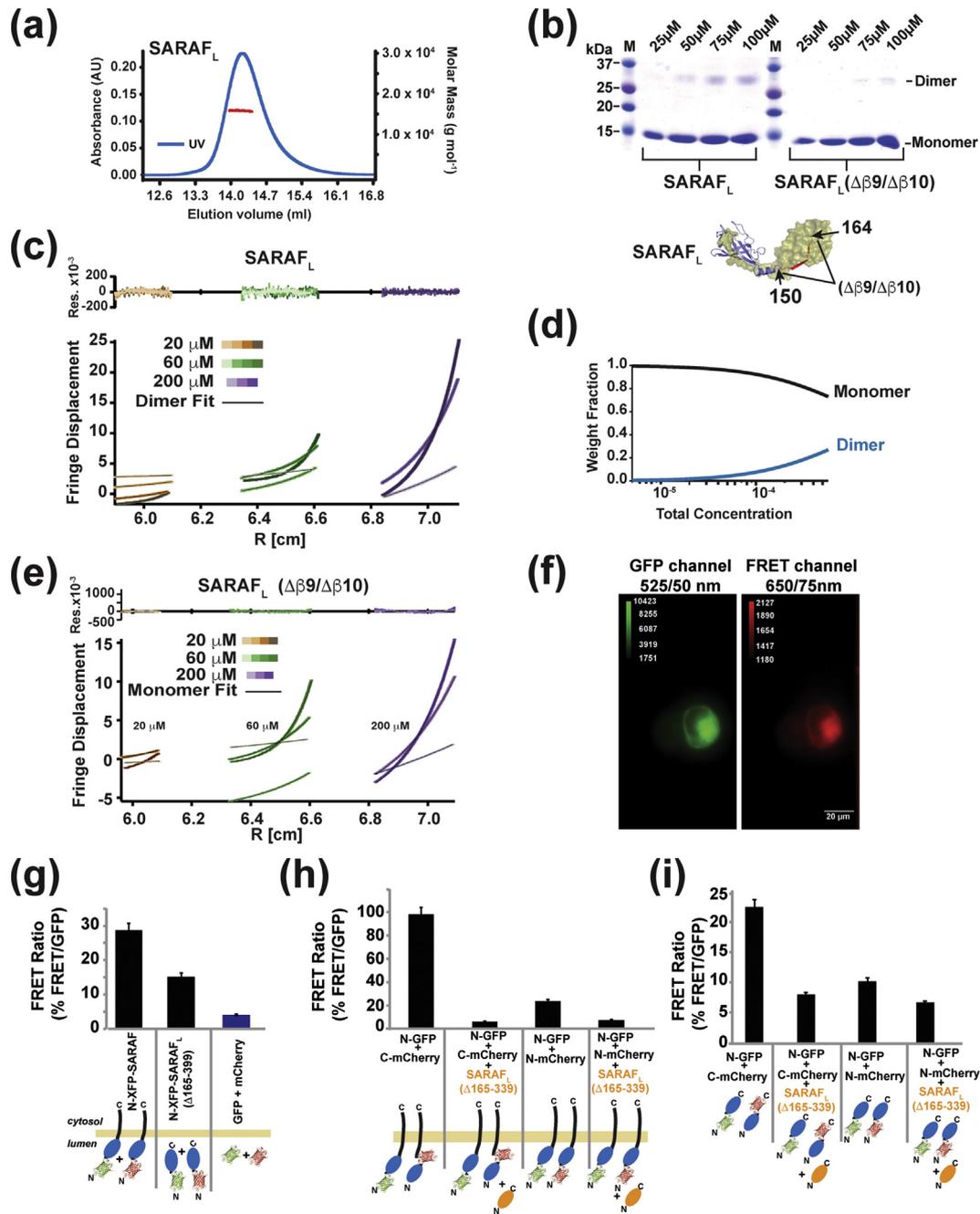
Fig. 5. SARAF self-association requires the SARAF luminal switch domain. (a) SEC-MALS of 64 μM (1 mg ml^{-1}) SARAF$_L$ (experimental Mw 15.84 kDa ± 0.08, Mw/Mn = 1.000 ± 0.007, predicted monomer Mw 15.49 kDa). (b) SDS-PAGE of glutaraldehyde crosslinked SARAF$_L$ and SARAF$_L$ (Δβ9/β10) as a function of protein concentration indicates SARAF$_L$ dimerization. (c) Equilibrium ultracentrifugation of SARAF$_L$ at the indicated concentrations. Rotor speeds of 10K, 18K, 22K, and 31K rpm are denoted by increasingly darker shades for each concentration. Residuals show fits to a monomer–dimer self-association model. (d) Calculated fraction of monomer and dimer SARAF$_L$ species as a function of concentration. (e) Equilibrium ultracentrifugation of SARAF$_L$ (Δβ9/β10) at the indicated concentrations. Rotor speeds of 10K, 18K, 22K, and 31K rpm are denoted by increasingly darker shades for each concentration. Residuals show fits to a single species model. (f) Example of images taken of cells expressing GFP-SARAF and mCherry-SARAF using DualView. The red channel is the FRET signal. (g) Bar graph describing the FRET/GFP signal ratio of acquired images as described in panel f. Fluorescent tags are fused N-terminally to SARAF or SP-SARAF$_L$-R [SARAF luminal domain (Δ165–339) with a signal peptide, SP, and an ER retention signal, R]. Signals from cells expressing monomeric SP-GFP-R and SP-mCherry-R are used to establish the background signal. (h) SP-SARAF$_L$-R (orange) inhibits the FRET signals between XFP-SARAF and (i) N-terminally tagged, SP-XFP-SARAF$_L$-R, or C-terminally tagged, SP-SARAF$_L$-XFP-R, luminal domains. For panels g–i, *** denotes $p < 0.001$. n for each combination is denoted above the bars.

that were indicative of a poor fit and the formation of a higher-order species (Fig. S4d). Accordingly, the SARAF$_L$ data could be well fit with a monomer–dimer association model (Fig. 5c and d), as indicated by the uniformly stochastic residuals. This analysis yields an estimate of the SARAF$_L$ dissociation constant in the low millimolar range (K_d ~ 2 mM). Such a value is entirely in line with the observation that SARAF$_L$ is monomeric under the low micromolar concentrations conditions used for SEC-MALS (Fig. 5a). In contrast to the behavior of SARAF$_L$, equilibrium analytical sedimentation studies of SARAF$_L$(Δβ9/Δβ10), which lacks the ability to form domain-swapped dimers, showed that this construct behaved as a monomeric protein that was well fit by a single species model (Fig. 5e). Together with the crosslinking studies, these data demonstrate that the domain swap of the SARAF$_L$ β9/β10 element is essential for dimerization.

SARAF self-associates in the ER

Given that purified SARAF$_L$ forms dimers solution, we sought to probe the extent to which such an interaction might occur in the context of a cell. We transfected HEK293 cells with equal amounts of full-length SARAF constructs bearing the fluorescent proteins, green fluorescent protein (GFP) [30] or mCherry [31], fused to the SARAF N-terminus (GFP-SARAF and mCherry-SARAF) and measured the FRET between the two constructs. We determined the amount of FRET by measuring the fluorescence emitted from mCherry under exclusive excitation of GFP, using Dual-View imaging, and quantified as the ratio of the red to green fluorescent intensities (FRET signal) (Fig. 5f). We then used a similar approach with N-terminally-tagged soluble luminal domains SARAF(Δ165-339) that lacked the trans-membrane anchor and that were targeted to the ER lumen by bearing both the SARAF signal peptide (SP) and a C-terminal retention signal (KDEL). FRET signals from the GFP-SARAF(Δ165–339) and mCherry-SARAF(Δ165–339) pair were substantially smaller than the GFP-SARAF and mCherry-SARAF pair but were still well above background (Fig. 5g). These results suggest that, in line with the biochemical studies, the SARAF luminal domains self-associate in the ER. This association happens whether the luminal domain is soluble form confined to the ER or is membrane anchored. The stronger FRET signals from the full-length constructs indicate that membrane anchoring enhances the luminal domain effective concentration [32,33] and facilitates self-association.

Because of the domain-swapped SARAF$_L$ dimer architecture, there is a much shorter distance between the N-and C-termini of the dimer partners (19.6 Å, Cα–Cα) than between the N- and C- termini of an individual subunit (66.7Å, Cα–Cα) or the N- and

C-termini of the dimer partners (75.4 Å and 61.8 Å, respectively) (Fig. S4e). These constraints predict that FRET signals will be larger between constructs in which the fluorophores are placed on opposite termini of the tested pairs (i.e., N-donor and C-acceptor). In line with this prediction, FRET between the GFP-SARAF$_L$:SARAF$_L$-mCherry pair was ~ 3-fold larger than the FRET signals observed from co-expressed pairs having each fluorophore fused to the SARAF$_L$ N-terminus, GFP-SARAF and mCherry-SARAF (Fig. 5h). Furthermore, in both cases, co-expression of untagged SARAF(Δ165–339) reduced the FRET signals to background levels, indicating that the FRET signals derive from co-association of the test proteins (Fig. 5i). Together, these data strongly support the notion that the domain-swapped form of the SARAF$_L$ occurs in a cellular context, forms in the full-length protein in cell membranes, that similar to in solution, self-association is reversible.

Design and characterization of SARAF$_L$ "Cys-lock" mutants identifies the SARAF luminal switch domain

The crosslinking and sedimentation equilibrium studies suggest that domain-swapped dimer exchanges freely with the monomeric state. In order to characterize properties of the monomer and dimer forms separately, we set out to create a SARAF$_L$ mutant that would be incapable of domain swap. We reasoned that incorporation of a fourth disulfide bond between the swapped strand and the core of SARAF$_L$ structure could serve as a "Cys-lock" that would covalently tether the swapped β9/β10 strand to the body of the protein. We identified a residue pair, Lys98–Ala156 on strands β6 and β9, as having favorable geometry to form such a disulfide when each member was mutated to cysteine. Purification of SARAF$_L$ K98C/A156C by ion exchange chromatography revealed the presence of two species corresponding to monomer and dimer forms present in a ratio of ~ 10:1 (Fig. S4f) and having different mobilities on size exclusion chromatography (Fig. 6a). SDS-PAGE under non-reducing conditions revealed two, separate species that ran at molecular weights consistent with the monomeric form (15.5 kDa) and the dimeric form (31.0 kDa). By contrast, both species ran identically upon addition of reducing agent (Fig. 6b), indicating that the two forms are the disulfide linked dimer (16.5 ml form) and disulfide linked monomer (18.3 ml form), respectively (Fig. 6a).

Both SARAF$_L$ K98C/A156C forms produced crystals that diffracted X-rays to high resolution, 1.58 and 2.1 Å for the monomer and dimer, respectively (Table S1). Molecular replacement using the SARAF$_L$ core lacking the surface loops and the β9/β10 strand revealed clear electron density in both structures for the engineered K98C/A156C "Cys-lock"
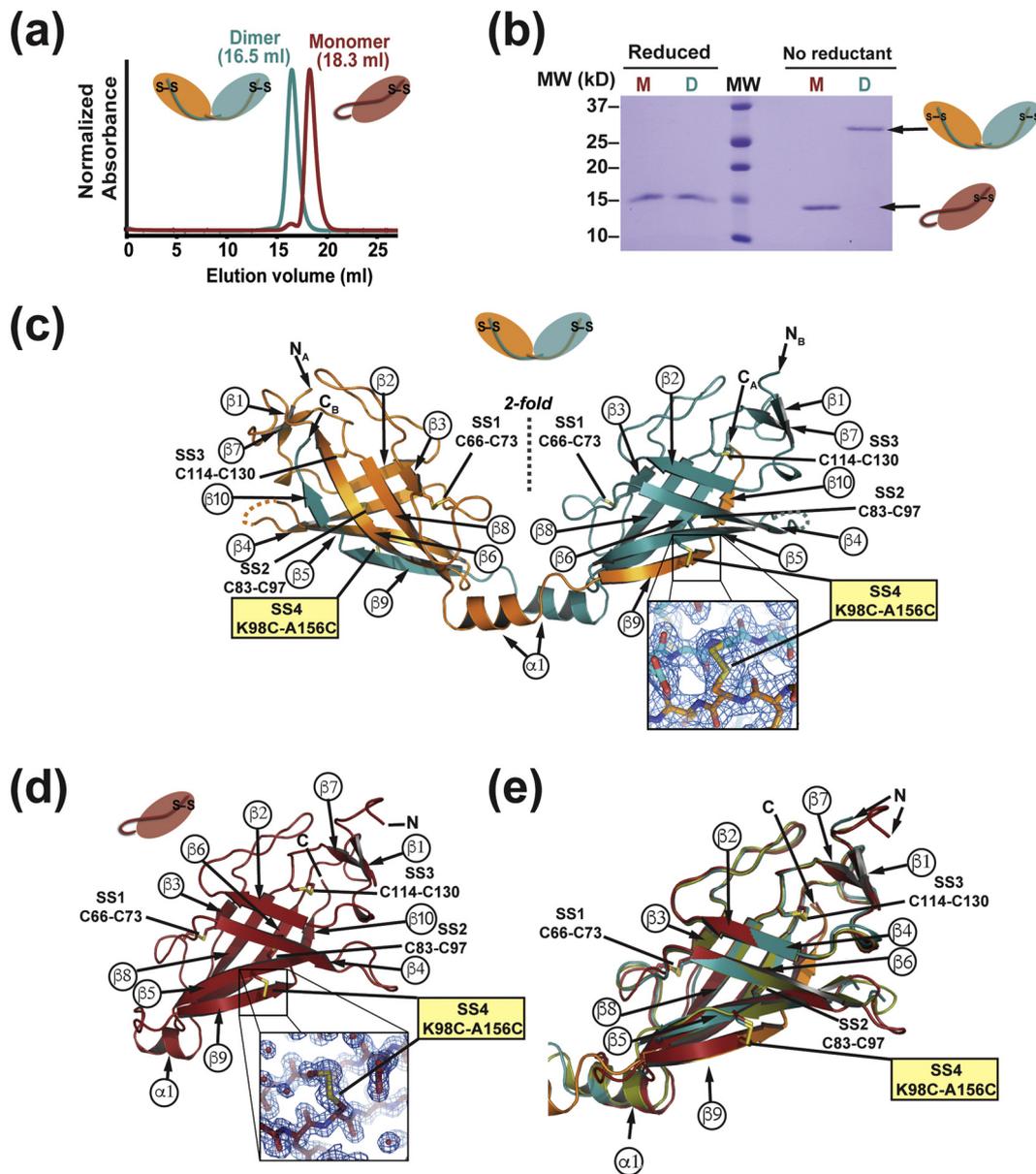
Fig. 6. Characterization and structures of Cys-locked SARAF$_L$ mutants. (a) Size exclusion chromatography profiles monomer and dimer species of SARAF$_L$ K98C/A156C. The Cys-locked dimer species elution profile is shifted earlier, consistent with a larger hydrodynamic radius. (b) SDS-PAGE gel of purified SARAF$_L$ K98C/A156C monomer (M) and dimer (D) species. The dimer band collapses to the same size as the monomer band upon addition of reducing agent (βME). (c) Crystal structure of the Cys-locked SARAF$_L$ K98C/A156C dimer showing the same topology and disulfide bonding as wild-type SARAF$_L$. Inset shows electron density (blue mesh, 1.5σ) for the engineered extra fourth disulfide bond (SS4). (d) Crystal structure of the Cys-locked SARAF$_L$ K98C/A156C monomer again showing the same strand arrangement and topology as wild-type SARAF$_L$ with the exception of β9 and β10 inserting in cis into the monomer β-sheet. Inset shows electron density (blue mesh, 1.5σ) for the engineered fourth disulfide bond (SS4). (e) Superposition of wild-type SARAF$_L$ (smudge green), Cys-locked SARAF$_L$ K98C/A156C dimer protomers (orange and deep teal), and Cys-locked SARAF$_L$ K98C/A156C monomer (firebrick red) showing the fold conservation across all three structures.

disulfide (Fig. 6c and d). Model building and refinement revealed that the Cys-lock monomer and Cys-lock dimer protomer maintain the same overall fold as the wild-type SARAF$_L$ dimer protomer (Fig. 6e) (RMSD$_{C\alpha}$ = 0.739 and 0.590 for residues 33–145 of the Cys-lock monomer and Cys-lock dimer *versus*

SARAF$_L$, respectively). Notably, the SARAF$_L$ K98C/A156C Cys-lock monomer has the marked difference that the tail, which extends from the core in the dimeric form, is wrapped under the bottom of SARAF$_L$ so that β9/β10 inserts in *cis* to complete the anti-parallel and mixed β-sheets of the SARAF$_L$ fold

(Fig. 6d). The α_1 helix is retained despite this topology change of the SARAF$_L$ tail, although it is shorter by one helical turn relative to the dimer form. In both the Cys-locked dimer and the Cys-locked monomer, the electrostatic surface potentials were very similar to wild-type SARAF$_L$ (Fig. S5). These structural studies demonstrate that the switch from monomer to dimer requires changes only in the β9/β10 tail and not the SARAF$_L$ core. Accordingly, we term the β9/β10 tail as the "SARAF luminal switch domain."

SARAF dimerization affects SOCE inactivation

To test the functional importance of the SARAF luminal switch, we used whole-cell patch clamp to measure SOCE currents from HEK293 cells that were co-transfected with Orai1-CFP and STIM1-mCherry along with GFP tagged version of SARAF, SARAF-GFP, or a SARAF mutant lacking the luminal switch, SARAF (Δβ9/β10)-GFP. Recording conditions included 1,4-dihydroxy-2,5-di-*tert*-butylbenzene, a reversible SERCA inhibitor, to allow for both depletion and refilling of Ca^{2+} stores. Because we observed a direct relationship between STIM1 expression level and Orai1 current density (Fig. S6), we limited our analysis to cells expressing STIM1-mCherry at or below a threshold of 5000 fluorescence counts/cell to ensure that any functional effects were not due to exceptionally high levels of STIM1. Cells expressing SARAF-GFP or SARAF (Δβ9/β10)-GFP had comparable levels of STIM1 expression (Fig. 7a and b) and similar passive membrane properties. However, we observed that the SOCE current densities 18s after addition of external Ca^{2+} to activate the current were roughly twice as large in cells expressing SARAF(Δβ9/β10)-GFP *versus* SARAF-GFP [42.6 ± 7.5 pA/pF (n = 9) and 21.2±4.3 pA/pF (n = 11), $p < 0.05$, respectively] (Fig. 7c). Furthermore, the time to maximum response for SOCE current activation was faster by ~2-fold in cells expressing the SARAF luminal switch mutant [17.1 ± 1.7 s and 32.5 ± 4.6 s (n = 11) and (n = 9), $p < 0.01$, for SARAF (Δβ9/β10)-GFP and SARAF-GFP, respectively] (Fig. 7d). These results indicate that the self-associated form of SARAF accelerates SOCE inactivation and that domain swap of the luminal switch is important for stabilizing this state.

Discussion

SARAF is a transmembrane, ER-resident, negative regulator of SOCE [24]. Understanding how it influences SOCE has been limited due to its lack of similarity to proteins of known structure. Crystallographic determination of the structure of the SARAF luminal domain, SARAF$_L$, shows that this domain comprises a novel, 10-strand β-sheet fold

constrained by three conserved disulfides that we name the "SARAF-fold." Although, the SARAF fold belongs to a class of β-sheet sandwich proteins represented by the γ-COPI appendage domain (1R4X), Xenavidin (2UYW), Avidin-related protein 2 (1WBI), and a *B. anthracis* conserved domain (3FBQ) (Fig. 3), the SARAF fold and topology are unique. Homologs having all six cysteines that form the three SARAF$_L$ disulfides as well as many conserved core residues in the SARAF$_L$ core occur in all five vertebrate classes (mammals, birds, amphibians, fish, and reptiles), including quite ancient members of this phylum, such as the sea lamprey (*P. marinus*) and coelacanth (*L. chalumnae*) (Figs. 1b and 4a and S2). Although SARAF$_L$ is widespread among vertebrates, it appears to be absent from other metazoans. Intriguingly, we found a set of fungal transmembrane proteins that are also SARAF$_L$ homologs (Figs. 4b and S3). This unusual distribution of homologs in both vertebrates and fungi establishes that the previously unknown SARAF-fold is widespread. Because fungi are not known to use the SOCE pathway, it seems likely that the SARAF-fold has other functions beyond its role in SOCE regulation.

Apart from its unique fold, our structural studies revealed a second key feature of the SARAF$_L$ fold, the ability to domain-swap. The formation of intertwined protein assemblies by exchange of identical structural elements is observed in many classes of soluble and transmembrane proteins [34–37]. Although this phenomenon provides a straightforward mechanism for homo-oligomer formation, its functional relevance is often not clear [34,37,38]. In SARAF$_L$, the swapped domain is a simple element comprising the β9 and β10 β-strands that insert into the essentially rigid, stable core of the rest of the fold.

Two structure-based protein design strategies firmly establish that the β9/β10 strands form the dimerization element. First, design of SARAF$_L$ mutant lacking β9 and β10 yielded a well-folded, stable protein that only differed from SARAF$_L$ in its inability to dimerize. Second, structure-based design to incorporate a disulfide between β9 and the SARAF$_L$ core yielded two covalently trapped species, a covalent dimer and a self-ligated monomer. Structural studies show that apart from the topological change, these two forms are identical. The intrinsic affinity of SARAF luminal switch-mediated dimerization is modest having a dissociation constant in the low millimolar range (K_d ~ 2 mM). Nevertheless, the transmembrane nature of full-length SARAF clearly imposes diffusional restrictions that serve to increase the effective concentration [32,33] and favor self-association (Fig. 5g). Importantly, overexpression of non-membrane anchored SARAF$_L$ is able to suppress the amount of dimer, indicating that full-length SARAF self-association is reversible (Fig. 5h). Hence, we term the β9/β10 element as the "SARAF luminal switch" domain, as biochemically this is the sole element
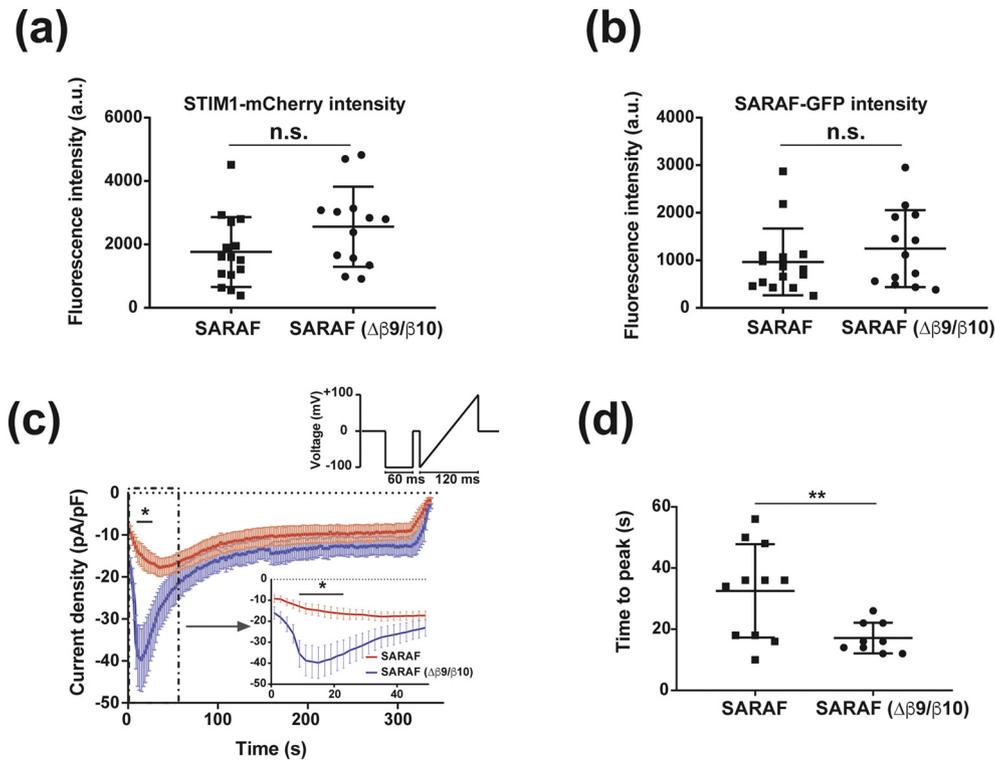
(a)

(b)

(c)

(d)

Fig. 7. Self-associated SARAF accelerates SOCE inactivation (a) STIM1-mCherry and (b) SARAF-GFP expression measured by fluorescence using epifluorescence illumination of cells expressing Orai1-CFP, STIM1-mCherry and SARAF-GFP, or SARAF ($\Delta\beta9/\Delta\beta10$)-GFP. (c) Average La^{3+}-sensitive current densities of HEK293 cells expressing Orai1-CFP, STIM1-mCherry, and SARAF-GFP or SARAF ($\Delta\beta9/\Delta\beta10$)-GFP measured at the end of 60-ms hyperpolarizing pulse to -100 mV in the presence of 10 mM extracellular Ca^{2+}. Inset shows the first 50 s of recording. Stimulation protocol is shown and was applied at 0.5 Hz. (d) Time to peak measured following the application of 10 mM Ca^{2+} for SARAF and SARAF ($\Delta\beta9/\Delta\beta10$). n = 11 and 9, respectively. $*p < 0.05$; $**p < 0.01$; n.s., not statistically different. Error bars indicate s.e.m.

required to convert between monomeric and dimeric forms and this domain is necessary for self-association of SARAF in membranes.

A hallmark of the SOCE pathway is that it is governed by reversible self-association of the ER sensor, STIM, in response to changes in ER calcium levels [15,17–22]. SARAF functional studies indicate that domain-swap mediated self-association is key for the ability of SARAF to accelerate inactivation of the SOCE current (Fig. 7). Whether, as with STIM1, SARAF also forms higher-order oligomers remains to be elucidated. In this regard, it is worth noting that crystal packing of $SARAF_L$ shows a simple face-to-face arrangement in which the C-termini that link $SARAF_L$ to the transmembrane portion all face the same direction (Fig. S1b). Such an arrangement would be compatible with formation of higher-order assemblies of SARAF dimers in the context of the membrane. Nevertheless, although the self-associated form of $SARAF_L$ is a dimer in both the crystal structure and in solution, non-symmetric domain swapping via the SARAF luminal switch could also form higher-order domain-swapped assemblies as has been observed in other domain-swapped proteins [38]. Hence, although SARAF clearly self-associates in the membrane

(Fig. 5g–i), and this association is important for function, the stoichiometry of self-organization and how such assemblies might be affected by interactions with STIM or Orai requires further investigation.

Initial characterization of SARAF demonstrated that it acts in a calcium-dependent manner, inhibiting SOCE only when ER stores were refilled with calcium [24]. $SARAF_L$ has no identifiable Ca^{2+}-binding motifs, and despite being crystallized in 1 mM $CaCl_2$, there is no evidence for non-canonical binding sites for Ca^{2+} on $SARAF_L$. Hence, how SARAF senses and responds to ER Ca^{2+} changes remains to be discovered. Given the absence of Ca^{2+} binding to $SARAF_L$, it may be that there is some type of Ca^{2+}-mediated interaction of $SARAF_L$ with the membrane inner leaflet or Ca^{2+}-dependent control of SARAF by a yet to be defined ER Ca^{2+}-sensor protein.

SOCE is a complex, multicomponent process that involves the reversible, coordinated association of proteins in both the ER and PMs [15]. The ER resident transmembrane protein SARAF serves an important role in this phenomenon by fine-tuning SOCE activity in response to ER refilling with Ca^{2+}. The discovery that the SARAF luminal domain

has a unique, disulfide-bonded β-sheet protein fold, capable of domain-swap mediated self-assembly that impacts function sets a key structural framework for understanding the basic roles of SARAF in controlling SOCE and the possible roles for SARAF in cancer, neurodegenerative diseases, and cardiomyopathy [39–43].

Materials and Methods

Protein expression and purification

Human SARAF$_L$ (residues 30–164) or SARAF$_L$ (Δβ9/Δβ10) (residues 30–150) were cloned into a modified version of the pET28 vector containing an N-terminal combination His$_6$ and maltose binding protein tag followed by TEV protease site (HMT). Point mutants were introduced using site-directed mutagenesis. The SARAF$_L$ or SARAF$_L$(Δβ9/Δβ10) constructs were transformed into SHuffle Express cells (NEB) and grown in 1 L cultures of 2YT media at 37 °C. The SHuffle Express cells have deletions of the genes for glutaredoxin reductase and thioredoxin reductase (*Δgor ΔtrxB*), which allow disulfide bonds to form in the cytoplasm. In addition, they constitutively express a chromosomal copy of the disulfide bond isomerase DsbC allowing for rearrangement of improperly oxidized disulfides. Cultures were induced with 0.5 mM IPTG at an OD$_{600nm}$ of ~0.6 and moved to 24 °C. Protein was expressed overnight, and cells were harvested by centrifugation and then immediately flash frozen in liquid nitrogen and stored at −80 °C. Frozen cell pellets were thawed on ice and resuspended in lysis buffer [25 mM HEPES (pH 7.4), 300 mM KCl, 1 mM CaCl$_2$, 10 mM Imidazole, 1 mM PMSF, 1 μg ml^{-1} DNaseI] at a ratio 6 ml lysis buffer to 1 g cell pellet. Resuspended cells were disrupted by sonication and insoluble material pelleted by centrifugation. Clarified lysate was mixed with 2 ml bed volume of Talon beads (Clontech) and incubated while rocking for 1 h at 4 °C. Following incubation, beads and lysate were transferred to a gravity flow column at washed with 2 × 30 ml lysis buffer before eluting with 15 ml lysis buffer containing 400 mM imidazole. After elution, protein was digested overnight with TEV at 4 °C and buffer exchanged into 10 mM Tris (pH 8.8) 10 mM KCl over a HiPrep desalting column. Desalted SARAF was then passed over a POROS MC20 column followed by an Amylose column to remove TEV and cleaved MBP. SARAF was further purified by MonoQ ion exchange before final gel filtration in 10 mM HEPES (pH 7.4), 200 mM KCl, and 1 mM CaCl$_2$ and concentrated to 10 mg ml^{-1} for crystallization.

The double mutant SARAF$_L$ K98C/A156C was expressed and purified following the same protocol as wild-type protein with the separation of monomer and dimer populations occurring at the ion exchange step before proceeding on to gel filtration. SARAF 31-164 K98C/A156C monomer and dimer were concentrated to 10 and 4 mg ml^{-1}, respectively, prior to crystallization.

Crystallization and data collection

Crystals used for structure determination of the wild-type construct were grown in 0.1 M BisTris (pH 6.5) and 18%–20% PEG 5000 MME in hanging drop format. Crystallization drops were set over a thin layer of vacuum grease to prevent crystals from sticking to the coverslips and facilitate harvesting. Harvested crystals were cryoprotected by sequential soaks in mother liquor plus 5%, 10%, 15%, and 20% glycerol before flash cooling in liquid nitrogen. For experimental phasing, crystals were soaked with 1 mM K$_2$Pt (NO$_2$)$_4$ overnight before back-soaking into mother liquor and cryoprotecting in glycerol as above. Crystals of SARAF 30–164 K98C/A156C monomer were grown in 0.1 M sodium acetate (pH 4.2–4.6) and 1.2–1.6 M sodium formate in standard hanging drop format without the use of vacuum grease. Harvested crystals were cryoprotected by sequential soaks in mother liquor plus 5%, 10%, 15%, and 20% glycerol before flash cooling in liquid nitrogen. Crystals of SARAF 30–164 K98C/A156C dimer were grown in 3%–5% glycerol or ethylene glycol after first treating protein to mild heating at 37 °C for 5 min or ultracentrifigation (40,000 rpm, 30 min, 4 °C) to remove microcrystals that spontaneously form in concentrated protein solution. Harvested crystals were cryoprotected by directly soaking in 25% ethylene glycol before flash cooling in liquid nitrogen.

Data were collected at Advanced Light Source beamline 8.3.1. Native data sets of wild-type SARAF were collected at a wavelength of 1.127 Å and diffracted to 1.90 Å. Peak, inflection, and high remote data sets were collected from K$_2$Pt(NO$_2$)$_4$-soaked crystals and diffracted to a resolution of 2.15 Å. Native data sets for both SARAF K98C/A156C monomer and dimer were collected at a wavelength of 1.116 Å and diffracted to resolutions of 1.58 and 2.10 Å, respectively.

Data processing and structure determination

Data from both native and K$_2$Pt(NO$_2$)$_4$-soaked wild-type crystals were indexed, integrated, and scaled in spacegroup C2 using autoPROC [44]. autoSHARP [45] was used to determine initial experimental phases using peak, inflection, and remote data sets from K$_2$Pt(NO$_2$)$_4$-soaked crystals finding a total of 10 platinum sites. An initial model was obtained using ARP/wARP [46] and improved with iterative rounds of manual rebuilding with COOT [47] and refinement with Phenix [48]. The SARAF K98C/A156C monomer and dimer structures were phased by molecular replacement with PHASER

[49] using the wild-type structure with the tail and surface loops removed as a search model. As with the wild-type structure, the models were improved with iterative rounds of manual rebuilding in COOT [47] and refinement in Phenix [48].

Analytical ultracentrifugation

Sedimentation equilibrium experiments were performed at 4 °C in an Optima XL-I analytical ultracentrifuge (Beckman Coulter). Prior to loading the rotor cells, 500 µl of $SARAF_L$ or $SARAF_L(\Delta\beta9/\Delta\beta10)$ was dialyzed against 1 L of buffer [200 mM KCl, 10 mM HEPES, (pH 7.4)] overnight at 4 °C. 125 µl of $SARAF_L$ or $SARAF_L(\Delta\beta9/\Delta\beta10)$ were loaded into six chamber center pieces at three concentrations of 20, 60, and 200 µM determined by absorbance at 280 nm [50]. Dialysate buffer (115 µl) was loaded into adjacent reference chambers. Data were acquired using interference optics at rotor speeds of 10K, 18K, 22K, and 31K rpm. Data acquired at multiple loading concentrations and rotor speeds were modeled globally in IgorPro using a standard monomer–dimer self-association model. V_{bar} and solvent density were calculated using Sednterp, and the interference extinction coefficient was calculated using the formula $e_{int} = 2.733 \times MW$. For global fitting, Vbar, MW, solvent density, and e_{int} were held constant, while K_d (for $N = 2$) was allowed to float.

Glutaraldehyde crosslinking

Purified $SARAF_L$ or $SARAF_L(\Delta\beta9/\Delta\beta10)$ in a buffer of 10 mM HEPES, (pH 7.4) and 200 mM KCl at concentrations ranging from 25 to 100 µM, determined by absorbance at 280 nm [50], was combined with 0.01% glutaraldehyde (Aldrich) in a final volume of 10 µl and incubated at room temperature for 10 min. Reactions were quenched by adding 1 µl of 1 M Tris (pH 8.0) to achieve a final concentration of 100 mM and Tris (pH 8) and were then boiled for 10 min in reducing SDS-sample buffer prior. Samples were subsequently analyzed by SDS-PAGE.

SEC-MALS

Multi-angle light scattering (MALS) experiments were carried out at 4 °C using an HPLC (Shimadzu) with UV detector connected to a miniDAWN TREOS MALS detector and an Optilab T-rEX refractometer (Wyatt Technology). One hundred microliters of 1 mg ml^{-1} of purified $SARAF_L$ was injected onto a Superdex S200 10/300 GL column (GE Healthcare) equilibrated in 200 mM KCl and 10 mM HEPES, (pH 7.4), and eluted peak was detected online. Molecular weight was calculated at each time point during elution using a combination of UV absorbance, light scattering, and differential refractive index measurements with the Astra software package

(Astra 6.0, Wyatt Technology). The experimentally determined molecular weight of $SARAF_L$ of 15.84 kDa ($\pm 0.509\%$) compares well with the 15.49 kDa calculated from the protein sequence. $SARAF_L$ was monodisperse with a polydispersity ratio (Mw/Mn) of 1.000 ($\pm 0.719\%$).

Circular dichroism

Prior to measurement, 600 µl each of 10 µM $SARAF_L$ and 10 µM $SARAF_L$ ($\Delta\beta9/\beta10$), determined by absorbance at 280 nm [50], were dialyzed overnight at 4 °C against 1 L of 30 mM sodium phosphate buffer. Circular dichroism spectra were measured with a 1-mm path-length quartz cuvette using an Aviv model 215 spectropolarimeter (Aviv Biomedical) equipped with a Peltier temperature controller. Wavelength scans from 320 to 185 nm were taken at 1-nm intervals at 4 °C. Each scan was performed in triplicate from the same sample and subtracted by the average of a triplicate scan of the dialysate for a matched buffer blank. Molar ellipticity was calculated as follows: $\theta = 100(\Delta m)/(Cnl)$, where Δm is the CD signal in millidegrees after buffer subtraction, C is the millimolar peptide concentration, n is the number of residues in the peptide, and l is the cuvette path length in centimeters.

Cell culture

HEK293 cells were grown in DMEM supplied with fresh L-glutamine, sodium pyruvate, FBS, and penicillin/streptomycin. Cells were split to 35-mm plates 1 day prior to transfection. Transfection with 600 ng of C-terminally GFP-tagged SARAF or SARAF($\Delta\beta9/\beta10$), 200 ng of C-terminally mCherry-tagged STIM1, and 200 ng of C-terminally CFP-tagged Orai1 with PEImax reagent (Polysciences) was performed 22–36 h prior to imaging and electrophysiological experiments. Cells were transferred to poly-L-lysine covered 24-mm coverslips one night prior to the experiments.

FRET

Cells were excited with 470/40-nm light for FRET measurements, and fluorescent signals were collected through the objective and split using Dual-View device (565LP dichroic) to GFP (525/50) and mCherry (650/75) channels using EMCCD 512x512 (Princeton Instruments). Images were processed using SlideBook (Intelligent Imaging Innovations) software and exported as Microsoft Excel files. FRET signals were assessed by dividing the FRET (mCherry) channel by the GFP channel. GFP or mCherry was fused to the N-termini of $SARAF_L$ (XFP-$SARAF_L$) or SARAF full length (XFP-SARAF) using the following sequence: SARAF(M1–G30)-TG-XFP-RT-SARAF(W31–K164)-KDEL or SARAF(M1–G30)-TG-XFP-RT-SARAF(W31–R339), respectively.

Fusions of monomeric forms of GFP [30] or mCherry [31] were made at the end of the luminal domain (K164) of the SARAF$_L$ (SARAF$_L$-XFP) or full-length SARAF and were at position K164 using the following sequence: SARAF(1–164)-TG RPACKIPNDLKQKVMNH-XFP-KDEL or SARAF (M1–K164)-TGLGGGGSGGGGSGGGGSAAAR-PACKIPNDLKQKVMNH-XFP-LGGGGSGGGGSGGGGSAAASGLRS-SARAF (M173–R339), respectively. ER retention signal (KDEL) was added at the C-termini of all luminal SARAF constructs.

Electrophysiological recordings

Membrane currents were recorded under voltage-clamp conditions using the whole-cell patch-clamp configuration using an Axopatch 200B (Axon Instruments) amplifier. Patch pipettes were fabricated from borosilicate glass capillaries (2–5 MΩ). Signals were analog filtered using a 2-kHz low-pass Bessel filter. Data acquisition and analysis were done using pCLAMP 9 software (Molecular Devices). Current densities were calculated by normalizing currents to cell capacitance. The recording protocol consisted of a 60-ms hyperpolarizing step to -100 mV from 0 mV, followed by a 20-ms step to 0 mV, and a 120-ms ramp from -100 to $+100$ mV repeated at 0.5 Hz for 300 s. All data were leak-corrected using the current in lanthanum-containing solution. The EGTA (ethylene glycol-bis(β-aminoethyl ether)-N,N,N',N'-tetraacetic acid) internal solution contained 150 mM Cs aspartate, 8 mM MgCl$_2$, 1.2 mM EGTA, 10 mM HEPES, and 2 mM Mg-ATP. The pH was titrated to pH 7.2 with CsOH. The external solution contained 145 mM NaCl, 2 mM MgCl$_2$, 2.8 mM KCl, 10 mM CsCl, 10 mM HEPES, and 10 mM glucose. The pH of the external solution was titrated to pH 7.4 with NaOH. CaCl$_2$ (10 mM) and 100 μM EDTA (ethylenediaminetetraacetic acid) or 10 mM MgCl$_2$ and 1 mM EDTA were added to the external solution for high-Ca^{2+} or Ca-free solution, respectively.

Fluorescence was measured from images acquired using EMCCD 1024 × 1024 iXonUltra camera under epifluorescence, and analyzed with VisiView software (Visitron Systems GmbH). Cells were excited using Xcite Exacte (Excelitas technologies) using the following filters: excitation filters ET470/40 for GFP and FF01-580/14 for mCherry; Emitted light was filtered with BP536/40 for GFP and HQ650/75 for mCherry. Data are presented as mean ± S.E.M.

Accession numbers

Coordinates and structure factors for SARAF$_L$, SARAF$_{L.SS}$ monomer, and SARAF$_{L.SS}$ dimer are deposited with the RCSB under accession codes 6O2U, 6O2V, and 6O2W, respectively, and will be released immediately upon publication.

Appendix A. Supplementary data

Supplementary data to this article can be found online at https://doi.org/10.1016/j.jmb.2019.05.008.

References

[1] D.E. Clapham, Calcium signaling, Cell. 131 (2007) 1047–1058.

[2] B. Hille, Ion Channels of Excitable Membranes, 3rd ed Sinauer Associates, Inc., Sunderland, MA, 2001.

[3] M.J. Berridge, M.D. Bootman, H.L. Roderick, Calcium signalling: dynamics, homeostasis and remodelling, Nat. Rev. Mol. Cell Biol. 4 (2003) 517–529.

[4] E. Carafoli, L. Santella, D. Branca, M. Brini, Generation, control, and processing of cellular calcium signals, Crit. Rev. Biochem. Mol. Biol. 36 (2001) 107–260.

[5] R. Hodeify, F. Yu, R. Courjaret, N. Nader, M. Dib, L. Sun, et al., Regulation and role of store-operated Ca(2+) entry in cellular proliferation, in: J.A. Kozak, J.W. Putney Jr. (Eds.), Calcium Entry Channels in Non-Excitable Cells, CRC Press, Boca Raton, FL 2018, pp. 215–240.

[6] M.D. Cahalan, STIMulating store-operated Ca(2+) entry, Nat. Cell Biol. 11 (2009) 669–677.

[7] R.S. Lewis, The molecular choreography of a store-operated calcium channel, Nature. 446 (2007) 284–287.

[8] J.W. Putney Jr., A model for receptor-regulated calcium entry, Cell Calcium 7 (1986) 1–12.

[9] A.H. Shim, L. Tirado-Lee, M. Prakriya, Structural and functional mechanisms of CRAC channel regulation, J. Mol. Biol. 427 (2015) 77–93.

[10] S. Feske, A mutation in Orai1 causes immune deficiency by abrogating CRAC channel function, Nature. 441 (2006) 179–185.

[11] C. Peinelt, Amplification of CRAC current by STIM1 and CRACM1 (Orai1), Nat. Cell Biol. 8 (2006) 771–773.

[12] J. Roos, STIM1, an essential and conserved component of store-operated Ca2+ channel function, J. Cell Biol. 169 (2005) 435–445.

[13] J. Soboloff, STIM2 is an inhibitor of STIM1-mediated store-operated Ca2+ entry, Curr. Biol. 16 (2006) 1465–1470.

[14] M. Poteser, G. Leitinger, E. Pritz, D. Platzer, I. Frischauf, C. Romanin, et al., Live-cell imaging of ER–PM contact architecture by a novel TIRFM approach reveals extension of junctions in response to store-operated Ca(2+)-entry, Sci. Rep. 6 (2016), 35656.

[15] M. Prakriya, R.S. Lewis, Store-operated calcium channels, Physiol. Rev. 95 (2015) 1383–1436.

[16] R. Qiu, R.S. Lewis, Structural features of STIM and Orai underlying store-operated calcium entry, Curr. Opin. Cell Biol. 57 (2019) 90–98.

[17] Bird GS, Hwang SY, Smyth JT, Fukushima M, Boyles RR, Putney JW, Jr. STIM1 is a calcium sensor specialized for digital signaling. Curr. Biol. 2009;19:1724-9.

[18] P.G. Hogan, R.S. Lewis, A. Rao, Molecular basis of calcium signaling in lymphocytes: STIM and ORAI, Annu. Rev. Immunol. 28 (2010) 491–533.

[19] T. Kawasaki, I. Lange, S. Feske, A minimal regulatory domain in the C terminus of STIM1 binds to and activates ORAI1 CRAC channels, Biochem. Biophys. Res. Commun. 385 (2009) 49–54.

[20] K.P. Lee, Molecular determinants of fast Ca2+-dependent inactivation and gating of the Orai channels, Proc. Natl. Acad. Sci. U. S. A. 106 (2009) 14687–14692.

[21] M.M. Wu, J. Buchanan, R.M. Luik, R.S. Lewis, Ca2+ store depletion causes STIM1 to accumulate in ER regions closely associated with the plasma membrane, J. Cell Biol. 174 (2006) 803–813.

[22] Y. Zhou, The short N-terminal domains of STIM1 and STIM2 control the activation kinetics of Orai1 channels, J. Biol. Chem. 284 (2009) 19164–19168.

[23] A.B. Parekh, Regulation of CRAC channels by Ca(2+)-dependent inactivation, Cell Calcium 63 (2017) 20–23.

[24] R. Palty, A. Raveh, I. Kamisky, R. Meller, E. Reuveny, SARAF inactivates the store operated calcium entry machinery to prevent excess calcium refilling, Cell. 149 (2012) 425–438.

[25] L. Albarran, J.J. Lopez, L.J. Gomez, G.M. Salido, J.A. Rosado, SARAF modulates TRPC1, but not TRPC6, channel function in a STIM1-independent manner, Biochem. J. 473 (2016) 3581–3595.

[26] A. Jha, M. Ahuja, J. Maleth, C.M. Moreno, J.P. Yuan, M.S. Kim, et al., The STIM1 CTID domain determines access of SARAF to SOAR to regulate Orai1 channel function, J. Cell Biol. 202 (2013) 71–79.

[27] Z. Zhang, W.J. Henzel, Signal peptide prediction based on analysis of experimentally verified cleavage sites, Protein science : a publication of the Protein Society. 13 (2004) 2819–2824.

[28] L. Holm, P. Rosenstrom, Dali server: conservation mapping in 3D, Nucleic Acids Res. 38 (2010) W545–W549.

[29] E. Folta-Stogniew, Oligomeric states of proteins determined by size-exclusion chromatography coupled with light scattering, absorbance and refractive index detectors, Methods Mol Biol. 328 (2006) 97–112.

[30] D.A. Zacharias, J.D. Violin, A.C. Newton, R.Y. Tsien, Partitioning of lipid-modified monomeric GFPs into membrane microdomains of live cells, Science. 296 (2002) 913–916.

[31] N.C. Shaner, R.E. Campbell, P.A. Steinbach, B.N. Giepmans, A. E. Palmer, R.Y. Tsien, Improved monomeric red, orange and yellow fluorescent proteins derived from *Discosoma* sp. red fluorescent protein, Nat. Biotechnol. 22 (2004) 1567–1572.

[32] W.P. Jencks, Catalysis in Chemistry and Enzymology, Dover ed. Dover Publications, New York, NY, 1987.

[33] Creighton T.E. Proteins, Structures and Molecular Properties, 2nd ed W.H. Freeman and Company, New York, 1993.

[34] S.J. Wodak, A. Malevanets, S.S. MacKinnon, The landscape of intertwined associations in homooligomeric proteins, Biophys. J. 109 (2015) 1087–1100.

[35] M.J. Bennett, D. Eisenberg, The evolving role of 3D domain swapping in proteins, Structure. 12 (2004) 1339–1341.

[36] M.J. Bennett, S. Choe, D. Eisenberg, Domain swapping: entangling alliances between proteins, Proc. Natl. Acad. Sci. U. S. A. 91 (1994) 3127–3131.

[37] F. Rousseau, J. Schymkowitz, L.S. Itzhaki, Implications of 3D domain swapping for protein folding misfolding and function, Advances in experimental medicine and biology. 747 (2012) 137–152.

[38] S.S. Mackinnon, A. Malevanets, S.J. Wodak, Intertwined associations in structures of homooligomeric proteins, Structure. 21 (2013) 638–649.

[39] X. Chen, F. Long, B. Cai, X. Chen, G. Chen, A novel relationship for schizophrenia, bipolar and major depressive disorder. Part 7: a hint from chromosome 7 high density association screen, Behav. Brain Res. 293 (2015) 241–251.

[40] T.L. Romanuik, T. Ueda, N. Le, S. Haile, T.M. Yong, T. Thomson, et al., Novel biomarkers for prostate cancer including noncoding transcripts, Am. J. Pathol. 175 (2009) 2264–2276.

[41] T.L. Romanuik, G. Wang, R.A. Holt, S.J. Jones, M.A. Marra, M.D. Sadar, Identification of novel androgen-responsive genes by sequencing of LongSAGE libraries, BMC Genomics 10 (2009) 476.

[42] N.A. Twine, K. Janitz, M.R. Wilkins, M. Janitz, Whole transcriptome sequencing reveals gene expression and splicing differences in brain regions affected by Alzheimer's disease, PloS one 6 (2011), e16266.

[43] A. Camargo, F. Azuaje, Identification of dilated cardiomyopathy signature genes through gene expression

and network data integration, Genomics. 92 (2008) 404–413.

[44] C. Vonrhein, C. Flensburg, P. Keller, A. Sharff, O. Smart, W. Paciorek, et al., Data processing and analysis with the autoPROC toolbox, Acta Crystallogr D Biol Crystallogr. 67 (2011) 293–302.

[45] C. Vonrhein, E. Blanc, P. Roversi, G. Bricogne, Automated structure solution with autoSHARP, Methods Mol. Biol. 364 (2007) 215–230.

[46] G. Langer, S.X. Cohen, V.S. Lamzin, A. Perrakis, Automated macromolecular model building for X-ray crystallography using ARP/wARP version 7, Nat. Protoc. 3 (2008) 1171–1179.

[47] P. Emsley, B. Lohkamp, W.G. Scott, K. Cowtan, Features and development of Coot, Acta Crystallogr D Biol Crystallogr. 66 (2010) 486–501.

[48] P.D. Adams, P.V. Afonine, G. Bunkoczi, V.B. Chen, I.W. Davis, N. Echols, et al., PHENIX: a comprehensive Python-based system for macromolecular structure solution, Acta Crystallogr D Biol Crystallogr. 66 (2010) 213–221.

[49] A.J. McCoy, R.W. Grosse-Kunstleve, P.D. Adams, M.D. Winn, L.C. Storoni, R.J. Read, Phaser crystallographic software, J. Appl. Crystallogr. 40 (2007) 658–674.

[50] H. Edelhoch, Spectroscopic determination of tryptophan and tyrosine in proteins, Biochemistry 6 (1967) 1948–1954.